Catalase-integrated hyaluronic acid as nanocarriers for enhanced photodynamic therapy in solid tumor

Phua, Fiona Soo Zeng; Yang, Guangbao; Lim, Wei Qi; Verma, Apoorva; Chen, Hongzhong; Thanabalu, Thirumaran; Zhao, Yanli

2019

Phua, F. S. Z., Yang, G., Lim, W. Q., Verma, A., Chen, H., Thanabalu, T., & Zhao, Y. (2019). Catalase-integrated hyaluronic acid as nanocarriers for enhanced photodynamic therapy in solid tumor. ACS Nano, 13(4), 4742-4751. doi:10.1021/acsnano.9b01087

https://hdl.handle.net/10356/137637

https://doi.org/10.1021/acsnano.9b01087

Catalase Integrated Hyaluronic Acid as Nanocarriers for Enhanced Photodynamic Therapy in Solid Tumor

Soo Zeng Fiona Phua,[†] Guangbao Yang,[†] Wei Qi Lim,[†,‡] Apoorva Verma,[§] Hongzhong Chen,[†] Thirumaran Thanabalu,[§] and Yanli Zhao[†]*

[†]Division of Chemistry and Biological Chemistry, School of Physical and Mathematical Sciences, Nanyang Technological University, 21 Nanyang Link, Singapore 637371, Singapore

[‡]NTU-Northwestern Institute for Nanomedicine, Interdisciplinary Graduate School, Nanyang Technological University, 50 Nanyang Avenue, Singapore 639798, Singapore

[§]School of Biological Sciences, Nanyang Technological University, 60 Nanyang Drive, Singapore 637551, Singapore

ABSTRACT: Photodynamic therapy (PDT) as a treatment method has many advantages such as minimal invasiveness, repeatable dosage and low systemic toxicity. Issues with conventional PDT agents include the limited availability of endogenous oxygen and difficulty in accumulation at tumor site, which hindered the successful treatment of tumor. Herein, we developed catalase-encapsulated hyaluronic acid-based nanoparticles loaded with adamantane modified photosensitizer for enhanced PDT of solid tumor. Chlorin e6 (Ce6) as the photosensitizer was modified with adamantane to yield adamantane modified Ce6 (aCe6). The obtained nanosystem (HA-CAT@aCe6) could target overly expressed CD44 receptors on cancer cells, supplying oxygen by converting endogenous hydrogen peroxide (H_2O_2) to oxygen, and improving PDT efficacy upon the light irradiation. HA-CAT@aCe6 nanoparticles showed high colloidal stability and mono-dispersity in aqueous solution. The uptake and targeting property of HA-CAT@aCe6

were demonstrated by confocal microscopy and flow cytometry in MDA-MB-231 cell line possessing overly expressed CD44 receptors. The encapsulated catalase was able to decompose the endogenous H_2O_2 to generate O_2 *in situ* for relieving hypoxia in cells incubated under hypoxia conditions. Cell viability assays indicated that HA-CAT@aCe6 possessed minimal cytotoxicity in the dark, while presenting high cellular toxicity under 660 nm light irradiation at normoxic condition. As a result of the catalase capability in relieving hypoxia, HA-CAT@aCe6 also exhibited high cellular cytotoxicity under hypoxia condition. *In vivo* experiments revealed selective tumor accumulation of HA-CAT@aCe6 in MDA-MB-231 tumor bearing nude mice. Significant tumor regression was observed after intravenous injection of HA-CAT@aCe6 under light irradiation in comparison to the control system without loading catalase. Thus, HA-CAT@aCe6 demonstrated a great potential in overcoming hypoxia for targeted PDT.

KEYWORDS: catalase, drug delivery, hyaluronic acid, hypoxia, photodynamic therapy

Photodynamic therapy (PDT) in cancer treatment involves light illumination of appropriate wavelength on photosensitizers at the tumor site, converting endogenous molecular oxygen to cytotoxic singlet oxygen ($^1O_2$) *in vivo* for inhibition of tumor growth.[1-3] It has been extensively studied in the treatment of both premalignant and malignant skin tumours,[4,5] head and neck cancer,[6] prostate cancer,[2] non-small cell lung cancer and other cancers.[7] Advantages of PDT in cancer treatment include its minimal invasiveness in comparison to chemotherapy and radiotherapy, possible repeatable dose, and low systematic toxicity to the body.[1,8-10] Despite its extensive use in cancer treatment, the efficacy of PDT is still restricted by the penetration depth of low wavelength light in deep-situated tumor, non-specific accumulation of photosensitizers and

the lack of endogenous oxygen in tumor.[11] Hypoxia, a term used to describe the lack of oxygen,[12] arises in many solid tumors, particularly in regions that are far from the tumor blood vessels.[13] Many studies have been conducted on imaging[14] and therapy toward hypoxic tumor.[11] Hypoxic tumor is often resistant to drugs, thus limiting the chemotherapy efficacy.[15] PDT as a treatment approach also shows low efficacy on account of the hypoxia.

To date, different methods have been used for overcoming the limited supply of oxygen in tumors such as direct delivery of oxygen,[16,17] *in situ* generation of oxygen[18-22] and improving blood flow.[11,23] Specifically, *in situ* generation of oxygen using catalase as an enzyme is attractive because it is self-responsive to hydrogen peroxide (H_2O_2) and does not require pre-treatment with oxygen ($^3O_2$).[18,19,24] It has been shown that excessive reactive oxygen species (ROS) such as H_2O_2 are produced in cancer cells.[25] Catalase could catalyze H_2O_2 to $^3O_2$ for relieving hypoxia in solid tumor.[26] The production of oxygen could ameliorate tumor hypoxia, leading to better PDT efficacy. Delivery of proteins such as catalase raises a few concerns such as its instability *in vivo* due to the presence of numerous physiological proteases, unpredictable protein immunogenicity, and poor *in vivo* half-life.[27,28] Thus, design of suitable nanocarriers that can overcome these problems is highly needed.

Many researchers have tried to improve the protein stability by encapsulation them within inorganic nanoparticles (NPs).[29,30] These methods often involved complicated synthesis procedures and the inorganic materials used often have issues being metabolized. In contrast, using organic materials as nanocarriers lead to good biodistribution, easy metabolism and better biodegradablility.[31-34] PEGylation is widely used in such modification for the delivery of proteins/peptides into the human body.[35] Numerous advantages of such polymer modification include the improved stability, solubility and pharmacokinetics.[36,37] An example of the US Food

and Drug Administration (FDA) approved PEG-protein conjugates is Oncaspar (mPEG-L-asparaginase).[38] However, high molecular weight PEGylation has its disadvantage of poor biodegradability.[36] In light of this, polysaccharides such as dextran and hyaluronic acid (HA) as biodegradable polymers[36,39] have been explored for modifications on proteins. HA, a natural polysaccharide composed of alternate units of two sugar monomers *i.e.*, glucuronic acid and *N*-acetylglucosamine,[40] is biodegradable and biocompatible with high biosafety. HA is known to target the overly expressed CD44 receptors in several tumors including MDA-MB-231 human breast cancer[41] and A549 lung cancer.[42,43] In addition, HA is highly amenable to chemical functionalization due to the presence of reactive functional groups such as acetamide, aldehyde, carboxyl, and hydroxyl groups.[37] Many studies have been reported on using HA as a therapeutic carrier with covalently attached photosensitizers for targeted therapy.[44-46] On the other hand, such direct conjugation onto the polymer results in the difficulties in controlling the amount of photosensitizers delivered and prolonging the storage of light sensitive photosensitizers. Therefore, an alternative strategy as opposed to direct conjugation of photosensitizers should be devised.

Herein, we report a therapeutic system (HA-CAT@aCe6) consisting of (1) CD44-targeting HA, (2) catalase (CAT) as an enzyme to catalyze the production of H_2O and O_2 from endogenous H_2O_2, and (3) adamantane modified Chlorin e6 (aCe6) photosensitizer to produce $^1O_2$ from the ground state $^3O_2$ (Scheme 1). In this system, β-cyclodextrin was first functionalized onto HA, followed by conjugation with catalase to form HA-CAT NPs. It was hypothesized that the integration of HA with catalase improves physiological stability of the system in presence of body proteases, and at the same time, enables active targeting to tumor. aCe6 photosensitizer is loaded into HA-CAT by supramolecular means between β-cyclodextrin and adamantane to give HA-CAT@aCe6 that can

target tumors possessing overly expressed CD44 receptors. Such supramolecular loading enables separate storage of different components and easy adjustment of the loading ratio between photosensitizer and catalase, which is tunable and predictable.[47] Upon light irradiation, aCe6 in HA-CAT@aCe6 produces $^1O_2$ for PDT, even in hypoxic tumor. Some advantages of this system are (1) active targeting capability, (2) suitable nanosize for accumulation in tumor, (3) presence of catalase to produce oxygen for overcoming hypoxia in solid tumor, and (4) facile and controlled loading of photosensitizers using supramolecular means, all of which affording the enhanced PDT efficacy *in vivo*.

RESULTS AND DISCUSSION

Fabrication and Characterizations of HA-CAT@aCe6 NPs. Cyclodextrin-modified HA was synthesized by using 1-ethyl-3-(3-dimethylaminopropyl)carbodiimide (EDC) and N-hydroxybenzotriazole (HOBt) coupling. Low molecular weight HA (8 – 15 kDa) was conjugated to β-cyclodextrin to produce HA-CD with a conjugation degree of 6.56%. The photosensitizer Ce6 was modified with adamantane for easy loading with HA-CD *via* supramolecular means. The compounds synthesized were all characterized by ^{1}H NMR spectra (Figures S1-S4). Following which, HA-CD was reacted with catalase in different mass ratios of HA-CD:catalase (1:1, 3:1 and 6:1) *via* the EDC and HOBt coupling to produce HA-CAT. Catalase, an enzyme that catalyzes the production of O_2 from H_2O_2, was introduced for promoting the PDT efficiency in hypoxic tumor. HA-CD:catalase mass ratio of 3:1 was eventually chosen for further studies, since the obtained HA-CAT has a reasonable hydrodynamic diameter suitable for the accumulation in tumor[48] and better retained activity of catalase (Figure S5 and Table S1). The concentrations of catalase in all catalase-containing NPs were determined by the bicinchoninic acid (BCA) protein assay. The mass

amount of HA-CD to catalase was approximately 1.4:1 as determined by the subtraction of the catalase mass (measured by the BCA protein assay) from the known dried mass of HA-CAT. For the same concentration of catalase in HA-CAT and free catalase, the activity of HA-CAT was estimated to be 15.3% of free catalase, determined using the Amplex Red Catalase Kit. For controlled loading of photosensitizer, aCe6 was loaded into HA-CAT by simply mixing the known amount of aCe6 pre-dissolved in dimethyl sulfoxide, followed by the dialysis against phosphate-buffered saline (PBS) to give HA-CAT@aCe6. The loading was based on the formation of inclusion complex between adamantane on aCe6 and β-cyclodextrin modified on HA.

HA-CAT and HA-CAT@aCe6 NPs were fully characterized. Transmission electron microscopy (TEM) images show a spherical morphology for both HA-CAT and HA-CAT@aCe6 NPs (Figure 1a,b). HA-CAT NPs in water have a hydrodynamic diameter of 224.0 nm as measured by the dynamic light scattering (DLS) with zeta potential of -20.3 mV, while free catalase has a diameter of approximately 9.4 nm with zeta potential of -3.4 mV. The increase in size and reduction in zeta potential from highly negatively charged HA-CAT demonstrated the successful conjugation of HA-CD with catalase (Figure 1c,d). HA-CAT@aCe6 NPs are slightly larger with a hydrodynamic diameter of 233.6 nm and zeta potential of -13.6 mV (Figure 1c,d). Vertical gel electrophoresis was used to verify the successful synthesis of HA-CAT (Figure 1e). Catalase is made up of 4 monomeric proteins and gives a single 66 kDa band on sodium dodecyl sulfate polyacrylamide gel electrophoresis (SDS-PAGE) by taking the reference with the known mass of protein in lane 1 where lane 1 is the protein ladder. After the conjugation of HA-CD onto catalase to form HA-CAT, a trailing band was observed in the SDS-PAGE lane (lane 3), which was a result of the increased molecular weight of HA-CAT. After the photosensitizer loading, the presence of characteristic absorbance bands of aCe6 at around 400 nm and 660 nm with the aggregation-

induced blue shift confirmed the successful entrapment of aCe6 in HA-CAT@aCe6 NPs (Figure 1f). The entrapment efficiency of aCe6 by HA-CAT NPs ([catalase] = 40 μg/mL) was found to be 80.1 %. The final concentration of aCe6 was determined to be 9.7 μM by referencing to the standard calibration curve of aCe6 (Figure S6). The photosensitizer loading efficiency was found to be 2.0 % (w/w), with reference to the mass of HA-CAT.

Evaluation of Catalase Activity. Following the preparation of HA-CD and HA-CAT@aCe6 NPs, their abilities to generate O_2 when incubated with H_2O_2 (0.5 mM) were investigated. As shown in Figure 1g, H_2O_2 and HA@aCe6 NPs (control group without catalase loaded) did not have a significant effect on the generation of O_2 in the solution. The slight increase of the O_2 concentration in the H_2O_2 sample was probably caused by inherent decomposition of H_2O_2. On the other hand, HA-CAT and HA-CAT@aCe6 NPs produced significantly higher amounts of O_2 when incubated with H_2O_2. Comparatively, free catalases produced O_2 at the fastest rate, reaching the maximum concentration of O_2 at 90 s. HA-CAT and HA-CAT@aCe6 showed a steady increase in the O_2 concentration upon time. They did not show obvious differences in the production of O_2 from H_2O_2, suggesting that the photosensitizer loading did not affect the activity of catalase. The activities of HA-CAT and HA-CAT@aCe6 NPs were lower than that of free catalase, since the conjugation of HA-CD onto catalase made it less available for the catalytic reaction. Nonetheless, the capacity of HA-CAT and HA-CAT@aCe6 NPs is high enough for catalytic production of O_2 from H_2O_2.

Production of Singlet Oxygen. After the verification that O_2 could be produced from HA-CAT and HA-CAT@aCe6 NPs upon the addition of H_2O_2, we tested their efficiency in the generation of $^1O_2$ using singlet oxygen sensor green (SOSG). SOSG has weak fluorescence, but when it reacts with $^1O_2$, the fluorescence increases at 530 nm under the excitation at 494 nm. After the

modification of Ce6 with adamantane, the verification is needed to ensure that the obtained aCe6 is also able to produce $^1O_2$. When only H_2O_2 was present in the solution, no fluorescence was observed. Obvious fluorescence increase was measured for HA-CAT@aCe6 or aCe6 with H_2O_2 when irradiated under light, indicating their comparable $^1O_2$ production capability. Considering effective generation of oxygen *via* the catalysis of loaded catalase on H_2O_2, the production of $^1O_2$ by HA-CAT@aCe6 with H_2O_2 presented the highest fluorescence change at 530 nm at all irradiation time (Figure 1h). This observation indicates that the production of $^1O_2$ was enhanced in the presence of both catalase and H_2O_2, which could possibly promote the PDT efficacy of HA-CAT@aCe6 NPs *in vitro* and *in vivo*.

Stability of Conjugated Catalase. Catalase might rapidly lose its stability and activity *in vivo* during the blood circulation owing to the degradation by other enzymes especially the proteases. The conjugation of enzymes to polymers was known to improve the stability of the enzymes due to the polymer protection from the proteases.[37] To verify that the present modification could lead to better protein stability, free catalase or HA-CAT was incubated with proteinase K for a specific duration and their corresponding ability to decompose H_2O_2 was verified using the Gòth method.[49] As shown in Figure 1i, the activity of free catalase quickly decreased to near zero within 2 h after the incubation with proteinase K. In contrast, HA-CAT was still able to retain more than 90% of its activity after 2 h, and the activity remained high even after 4 h. Therefore, the conjugation of catalase with HA-CD polymer did improve its stability in the presence of proteinase K, which is important for tumor targeted delivery *in vivo*. The minimal change in the size of HA-CAT@aCe6 in different solutions (*i.e.*, PBS, cell culture medium, and deionized water) over three days also indicated its good physiological stability (Figure S7).

***In Vitro* Cellular Uptake and Cytotoxicity.** After verifying the sufficient capability of HA-CAT@aCe6 NPs for the $^1O_2$ production in the presence of H_2O_2, its cellular uptake in MDA-MB-231 breast cancer cells under both normoxic and hypoxic conditions was studied by the confocal microscopy and flow cytometry (Figure S8). Under both incubation conditions, the confocal images of MDA-MB-231 cells showed brighter fluorescence resulted from the loaded photosensitizer at longer incubation period, showing time-dependent uptake of HA-CAT@aCe6. Flow cytometric results also exhibited (Figure 2a) greater uptake of HA-CAT@aCe6 with longer incubation time by having higher mean fluorescence intensity (MFI). As HA was known to target CD44 receptors overexpressed on some cancer cells, the targeting ability of HA-CAT@aCe6 was verified by using $CD44^+$ MDA-MB-231 and $CD44^-$ MCF-7 cell lines. The levels of CD44 receptors on these cell lines were first evaluated, and $CD44^+$ MDA-MB-231 cells expressed greater amount of CD44 receptors as compared to $CD44^-$ MCF-7 cells (Figure S9a). Following the incubation of HA-CAT@aCe6 NPs with $CD44^+$ MDA-MB-231 and $CD44^-$ MCF-7 cells respectively (Figure S9b), the fluorescence from MDA-MB-231 cells was brighter as compared to that of MCF-7 cells at incubation times of both 2 h and 4 h. This result indicates that the uptake of HA-CAT@aCe6 by $CD44^+$ MDA-MB-231 cells was greater, probably through CD44 receptor-mediated endocytosis. Furthermore, competitive assay of HA was used to further support the targeting capability of HA-CAT@aCe6 (Figure S9c). Free HA with different concentrations (0, 5, 15, and 30 mg/mL) was incubated with MDA-MB-231 cells for 4 h before the addition of HA-CAT@aCe6. This process allowed the CD44 receptors on the cells to be occupied by free HA, and thus they were less available to facilitate the endocytosis of HA-CAT@aCe6. Indeed, with an increasing amount of free HA preincubated, the uptake of HA-CAT@aCe6 by both normoxic and

hypoxic cells decreased, confirming that the HA component in HA-CAT@aCe6 provides targeting property, enabling specific accumulation to CD44 receptor-overexpressed cancer cells (Figure 2b).

Then, immunostaining was used to measure the expression level of hypoxia induced factor 1α (HIF-1α) in MDA-MB-231 cells. HA-CAT@aCe6 NPs were incubated with the cells under hypoxic condition of 1% O_2. As shown in Figure 2c, high green fluorescence intensity was observed from the hypoxic cells, indicating the presence of HIF-1α proteins in the cells. Conversely, cells incubated with HA-CAT@aCe6 NPs showed less green fluorescence signal, indicating that the expression in HIF-1α was reduced and HA-CAT@aCe6 NPs were able to alleviate the hypoxia in the cells.

HA@aCe6 as a negative control was employed to investigate the catalytic effect of catalase in relieving hypoxia. TEM and DLS results of HA@aCe6 NPs showed that they were also suitable for cellular studies (Figure S10). Hypoxia/ROS detection assay was then conducted, and the cells were visualized using confocal microscopy under both normoxic and hypoxic conditions (Figures S11 and S12). Red fluorescence could be induced when the nitro group of the hypoxia detection probe is reduced to hydroxylamine and amino groups. Green fluorescence is induced by the conversion from 2',7'-dichlorofluorescein diacetate (DCFH-DA) to dichlorofluorescein (DCF) in the presence of ROS. The results showed that hypoxia could be relieved using either HA-CAT or HA-CAT@aCe6 NPs upon light irradiation under both normoxic and hypoxic conditions. The HA-CAT@aCe6 NPs were able to induce the greatest amount of ROS as shown by the highest intensity of green fluorescence from DCF.

In vitro cytotoxicity was studied to evaluate the therapeutic efficiency of different systems under normoxic (Figure 2d) and hypoxic (Figure 2e) conditions. When incubated with aCe6, HA@aCe6 and HA-CAT@aCe6 NPs at different concentrations (concentration of aCe6 was as high as 4.3

μM) in the dark, a little cytotoxicity was observed, showing high cell viability of over 90% in normoxic cells. The half maximal inhibitory concentration (IC_{50}) was computed to be 2.2 μM and 1.4 μM for HA@aCe6 and HA-CAT@aCe6 NPs under normoxic condition, respectively. The same study was conducted in hypoxic condition where the concentration of oxygen was set at 1%. The IC_{50} of HA@aCe6 increased to 4.8 μM, while the IC_{50} of HA-CAT@aCe6 drastically reduced to 0.72 μM under hypoxic condition (Figure S13). Comparing HA@aCe6 with the same concentration at normoxic and hypoxic conditions, its cytotoxicity greatly decreased at low concentration of oxygen under hypoxic condition. This is because the oxygen required for the generation of singlet oxygen to kill cancer cells was lower under hypoxic condition, thus impeding the therapeutic efficacy of the photosensitizer in HA@aCe6. On the contrary, HA-CAT@aCe6 at the same concentration under hypoxic condition still displayed high cell killing efficacy. At the same concentration of the photosensitizer in both HA@aCe6 and HA-CAT@aCe6 NPs with light irradiation, the cytotoxicity of HA-CAT@aCe6 NPs was greater than that of HA@aCe6. This outcome could be due to that the intrinsic H_2O_2 in cancer cells is catalyzed by catalase in HA-CAT@aCe6 to produce more O_2 for improving the PDT efficacy. HA-mediated cellular accumulation coupled with catalase-catalyzed oxygen production[25] from endogenous H_2O_2 increased the amount of singlet oxygen generated, promoting the cell killing efficacy of HA-CAT@aCe6 even under hypoxic condition. Therefore, HA-CAT@aCe6 was proven to be an efficient system for tumor-specific PDT.

***In Vivo* Biodistribution.** Before the application of HA-CAT@aCe6 NPs for *in vivo* PDT, its biodistribution was first investigated. aCe6, HA@aCe6 and HA-CAT@aCe6 NPs were individually injected into MBA-MD-231 tumor-bearing nude mice intravenously. With the use of *in vivo* fluorescent imaging system, the fluorescence signal at the tumor sites was monitored

(Figure 3a). At 2 h, the tumors of all treated mice showed similar fluorescence intensity. Upon time, the fluorescence intensity from aCe6 group decreased, while HA@aCe6 and HA-CAT@aCe6 groups showed an enhancement in fluorescence at 24 h time point (Figure 3a,b). After 24 h, the mice treated with HA-CAT@aCe6 NPs were sacrificed for *ex vivo* imaging of their major organs (Figure 3c). The tumors were found to show the highest brightness, translating to the highest accumulation of HA-CAT@aCe6 NPs in tumors (Figure 3d). Liver showed weaker fluorescence, and other major organs such as spleen, kidney, heart and lungs exhibited minimal fluorescence signal. Free Ce6 is not able to accumulate in the tumor site, since it is a small molecule and could diffuse in and out of the tumor freely, resulting in being metabolized.[50] On the other hand, both HA@aCe6 and HA-CAT@aCe6 NPs could accumulate in the tumor on account of the enhanced permeability and retention (EPR) effect.[51] The tumor-targeting ability of HA-CAT@aCe6 also facilitates its internalization.

After which, the ability of HA-CAT@aCe6 NPs to overcome hypoxia in tumors was also evaluated using fluorescent tagged antibody that binds to endogenous HIF-1α (green) and CD31 (red) on blood vessels.[52] Typically, the downregulation of both HIF-1α and CD31 indicates the relief of hypoxia in solid tumors. MDA-MB-231 tumors were sectioned and stained by fluorescent tagged antibody and visualized under the microscope. The tumors treated with HA-CAT@aCe6 NPs showed obviously alleviated hypoxia as compared to those without the treatment, as indicated by less intense fluorescence by HIF-1α and CD31. These immunofluorescence staining results indicate that HA-CAT@aCe6 NPs are indeed capable of overcoming hypoxia associated tumors for the PDT treatment.

***In Vivo* PDT.** Because of high accumulation of HA-CAT@aCe6 in tumor sites, its efficacy in the eradication of tumors was evaluated *in vivo* using nude mice bearing MDA-MB-231 tumors.

Five treatment groups comprising of five mice per group were monitored over a period of 14 days. The five treatment groups include I: control in which only PBS was injected, II: Free Ce6 with light irradiation, III: HA-CAT@aCe6 NPs in the dark, IV: HA@aCe6 with light irradiation, and V: HA-CAT@aCe6 NPs with light irradiation. The relative tumor growth curve was obtained as shown in Figure 4a. The tumor growth from group V was the most inhibited one among all groups, indicating the highest anti-tumor efficacy of HA-CAT@aCe6. On the other hand, HA@aCe6 NPs showed moderate inhibition of tumor growth because the accumulated NPs at the tumor site were not able to exhibit enough toxicity to ablate the whole tumor. This led to the continual growth of the tumor. On account of the non-accumulation of free Ce6 at tumor site, the irradiation of light did not result in the inhibition of tumor growth. HA-CAT@aCe6 NPs in the dark also showed little therapeutic efficacy. In general, all the systems administrated did not show any major systemic toxicity as the weights of the mice all maintained at a healthy level (Figure 4b). The tumors from all treatment groups were excised and weighed at the end of day 14. Group V had the lowest tumor mass, followed by groups IV, III, II and I (Figure 4c). The tumors in group V were the smallest among all the tumors (Figure 4d).

To further evaluate the anti-tumor efficacy of PDT using HA-CAT@aCe6 NPs, hematoxylin and eosin (H&E) stain and terminal deoxynucleotidyl transferase dUTP nick end labeling (TUNEL) were utilized to stain the tumors from groups I to V for histological analysis. Based on obtained results (Figure 4e), the most severe morphological change and necrosis from tumor slices were observed in group V, while moderate damages from group IV and minimal damages from groups I-III. For studying the systemic toxicity of HA-CAT@aCe6, healthy nude mice were injected with HA-CAT@aCe6 NPs and the major organs such as heart, liver, spleen, lung, and kidney were harvested for similar histological analysis. No major organ damage was observed

(Figure S15), indicating good biocompatibility of HA-CAT@aCe6. All in all, HA-CAT@aCe6 NPs displayed a great ability to target the tumor and reduce hypoxia in the tumor to ensure effective anti-tumor PDT.

CONCLUSION

In conclusion, we have successfully developed HA-CAT@aCe6 NPs capable of targeting CD44 overexpressed cancer cells and tumors as well as reducing the hypoxia to ensure high efficacy of PDT *in vitro* and *in vivo*. This method of catalase conjugation is feasible in protecting the catalase from the action of proteinase K. The protein stability was greatly enhanced through the conjugation with HA polymer. Thus, the loaded catalase was able to efficiently catalyze H_2O_2 to generate additional O_2 toward the production of ROS for PDT. Systemically administered HA-CAT@aCe6 NPs could selectively accumulate at tumor site and attenuate the tumor hypoxia for improved PDT. Therefore, HA-CAT@aCe6 NPs displayed a great potential as a therapeutic agent for tumor-targeted treatment. The present approach could be extended to other protein-based therapeutics or enzymes.

EXPERIMENTAL METHODS

Stability Evaluation of HA-CAT@aCe6 NPs. Stability of the NPs was tested under physiological conditions. The following conditions were employed: 1) PBS, pH 7.4 at 37 °C, 2) Dulbecco's modified eagle medium with 10% fetal bovine serum and 1% penicillin/streptomycin at 37 °C, and 3) deionized water at 37 °C. The zeta potential and hydrodynamic size of the NPs were monitored for three days.

Generation of O_2 from H_2O_2. To compare the O_2 generation ability of free catalase, HA-CAT, HA@aCe6 NPs, and HA-CAT@aCe6 NPs where [catalase] = 400 μg/ mL and [aCe6] = 90 μM, a solution of H_2O_2 (0.5 mM) was prepared. This concentration of H_2O_2 was chosen to ensure that the generated O_2 was detectable by the oxygen probe (Lovibond SD 400 OXI L). Endogenous H_2O_2 in the human body is about 100 μM.[53] The amount of HA-CAT@aCe6 used was proportionate to the catalase concentration used in cellular studies (40 μg/mL) and endogenous H_2O_2 concentration (approximately 100 μM). The increase in the O_2 concentration with respect to the initial O_2 concentration was calculated.

Catalase Activity Assay. To measure and compare the stability of free catalase and HA-CAT, the Góth method was used.[24] Both free catalase and HA-CAT with the final concentration of 300 μg/mL were incubated with Proteinase K (60 μg/mL) at 37 °C. At predetermined time points (0, 0.5, 1, 2, 3, 4 and 5 h), aliquots of samples were removed for immediate catalase activity assay. To determine the catalase activity, H_2O_2 (50 mM, 1 mL) was added with free catalase or HA-CAT (300 μg/mL, 0.2 mL) at 37 °C for 60 s, and then ammonium molybdate (32.4 mM, 1 mL) was added to terminate the reaction. The relative catalase activity was determined by the absorbance of the solution at 405 nm.

Detection of Singlet Oxygen. Singlet oxygen was determined by the following protocol.[24] In brief, SOSG dissolved in methanol was incubated with different samples ([SOSG] = 2.5 μM, [aCe6] = 4.9 μM, and [H_2O_2] = 0.25 mM) to measure singlet oxygen generation after light irradiation (630 nm, 15 mW/cm^2) purged under nitrogen. This amount of H_2O_2 was chosen to ensure that the generated $^1O_2$ could be detected by SOSG and the fluorescence of SOSG falls in the detection limit of our spectrometer. The generated $^1O_2$ was determined by measuring SOSG fluorescence signal at 528 nm under 494 nm excitation.

Immunofluorescence for Detection of HIF-1α in MDA-MB-231 Cells. MDA-MB-231 cells were seeded onto 6 well plates with cover slip and incubated at normoxic (21% O_2) and hypoxic (1% O_2) conditions for 24 h. HA-CAT@Ce6 NPs ([catalase] = 40 μg/mL, [aCe6] = 9 μM) were first incubated with the cells for 4 h. The cells were then quickly fixed with 4% paraformaldehyde at room temperature for 10 min, followed by washing with PBS thrice. The cells were permeabilized using 0.1% Triton X-100 in PBS for 10 min and washed thrice with 0.1% Tween-20 in PBS. After which, blocking buffer was added and incubated at room temperature for 1 h. The primary anti-HIF-1α antibody was diluted in blocking buffer (2:1000) to yield a final concentration (2 μg/mL) and incubated at room temperature for 1.5 h. The cells were washed thrice with 0.1% Tween-20 in PBS, and then incubated with the secondary Alexa Fluor®488-conjugated Goat Anti-Rabbit IgG H&L antibody diluted in blocking buffer (5:1000) with final concentration of 5 μg/mL at room temperature in the dark for 1 h. The sample was washed thrice with 0.1% Tween-20 in PBS. Finally, 4',6-diamidino-2-phenylindole (DAPI) with the working concentration of 300 mM was used to stain the nucleus for 3 min. The cells were washed and then visualized using the confocal microscopy with excitation wavelength of 488 nm and emission at 525 nm.

Immunofluorescence for Detection of CD44 Receptors in Different Cells. MDA-MB-231 and MCF-7 cells were seeded onto 6 well plates with the cover slip at the cell density of 200000 cells/well for 24 h, respectively. The cells were fixed with 4% paraformaldehyde at room temperature for 10 min, and then washed with PBS thrice. After which, the cells were permeabilized using 0.1% Triton X-100 in PBS for 10 min and washed thrice with 0.1% Tween-20 in PBS. Blocking buffer was added and incubated at room temperature for 1 h. The primary anti-CD44 antibody was diluted in blocking buffer (1:1000) to yield a final concentration (1 μg/mL) and incubated at room temperature for 1 h. The cells were washed with 0.1% Tween-20

in PBS thrice, and then incubated with the secondary Alexa Fluor®488-conjugated Goat Anti-Rabbit IgG H&L antibody diluted in blocking buffer (1:1000) with final concentration of 2 μg/mL at room temperature in the dark for 1 h. The system was washed with 0.1% Tween-20 in PBS thrice. Finally, DAPI with working concentration of 300 mM was used to stain the nucleus for 3 min. The cells were washed and then visualized using the confocal microscopy with excitation wavelength of 488 nm and emission at 525 nm.

***In Vivo* Studies.** For *in vivo* imaging, HA@aCe6 and HA-CAT@aCe6 NPs (200 μL) with an equivalent concentration of aCe6 (0.4 mg/mL) were intravenously injected into each mouse (aCe6 dose: 4 mg/kg). *In vivo* fluorescence imaging was carried out at wavelength of 675 nm and emission of 735 nm using an *in vivo* optical imaging system. The mice were sacrificed at 24 h after intravenous injection, having their major organs including heart, kidney, liver, lung, spleen, and tumor collected for *ex vivo* imaging. The fluorescence intensity was analyzed by ImageJ. To investigate the tumor hypoxia post treatment, BALB/c nude mice bearing MDA-MB-231 tumor were intravenously injected with HA-CAT@aCe6 NPs. After 24 h, the mice were injected with pimonidazole hydrochloride (hypoxyprobe-1 plus kit, 30 mg kg^{-1}) based on the procedure provided by the manufacturer. The mice were sacrificed after 90 mins for the collection of tumor slices for immunofluorescence staining. The slices were observed by the confocal microscopy.

For *in vivo* therapeutic studies, 25 tumor-bearing nude mice were randomly divided into five groups (five mice per group): I) control group with saline injection only, II) free Ce6 with light irradiation, III) HA@aCe6 NPs with light irradiation, IV) HA-CAT@aCe6 NPs in the dark, and V) HA-CAT@aCe6 NPs with light irradiation. The mice were injected with the materials, and after 24 h, groups II, III and V received light irradiation (50 mW/cm^2) on the tumor for 30 min. The doses of aCe6, catalase and Ce6 were 4 mg/kg, 18.4 mg/kg and 2.9 mg/kg, respectively. The

width and length of the tumors were measured using a digital caliper for 14 days. Tumor volumes were computed using the standard formula where volume = ½ × width^2 × height. The growth curve of the tumors was processed by comparing the tumor volume from each day to the initial tumor volume at day 0. Mice from each group were sacrificed at day 4 after the treatments to collect the tumors for evaluating the therapeutic effects.

ASSOCIATED CONTENT

Supporting Information

The Supporting Information is available free of charge on the ACS Publications website at DOI: 10.1021/acsnano.

Additional experimental details, synthesis and characterization, NMR spectra, DLS, zeta potential, TEM images, fluorescence images of cells, IC_{50} values, apoptosis assay, and H&E staining images (PDF)

AUTHOR INFORMATION

Corresponding Author

*Email: zhaoyanli@ntu.edu.sg

Author Contributions

The manuscript was written through contributions of all authors. All authors have given approval to the final version of the manuscript.

ACKNOWLEDGMENTS

This research is supported by the Singapore Academic Research Fund (No. RG5/16, RG11/17 and RG114/17), the Singapore Agency for Science, Technology and Research (A*STAR) AME IRG grant (No. A1883c0005), and the Singapore National Research Foundation Investigatorship (No. NRF-NRFI2018-03).

REFERENCES

(1) Dolmans, D. E. J. G. J.; Fukumura, D.; Jain, R. K. Photodynamic Therapy for Cancer. *Nat. Rev. Cancer* **2003,** *3*, 380-387.

(2) Moore, C. M.; Pendse, D.; Emberton, M. Photodynamic Therapy for Prostate Cancer—A Review of Current Status and Future Promise. *Nat. Clin. Pract. Urol.* **2009,** *6*, 18-30.

(3) Horrobin, D. F. *New Approaches to Cancer Treatment: Unsaturated Lipids and Photodynamic Therapy*; Churchill Livingstone: London, 1994.

(4) Ericson, M. B.; Wennberg, A.-M.; Larkö, O. Review of Photodynamic Therapy in Actinic Keratosis and Basal Cell Carcinoma. *Ther. Clin. Risk. Manag.* **2008,** *4*, 1-9.

(5) Tham, H. P.; Xu, K.; Lim, W. Q.; Chen, H.; Zheng, M.; Thng, T. G. S.; Venkatraman, S. S.; Xu, C.; Zhao, Y. Microneedle-Assisted Topical Delivery of Photodynamically Active Mesoporous Formulation for Combination Therapy of Deep-Seated Melanoma. *ACS Nano* **2018,** *12*, 11936-11948.

(6) Beasley, N. J.; Leek, R.; Alam, M.; Turley, H.; Cox, G. J.; Gatter, K.; Millard, P.; Fuggle, S.; Harris, A. L. Hypoxia-Inducible Factors Hif-1[Alpha] and Hif-2[Alpha] in Head and Neck Cancer: Relationship to Tumor Biology and Treatment Outcome in Surgically Resected Patients. *Cancer Res.* **2002,** *62*, 2493-2497.

(7) Agostinis, P.; Berg, K.; Cengel, K. A.; Foster, T. H.; Girotti, A. W.; Gollnick, S. O.; Hahn, S. M.; Hamblin, M. R.; Juzeniene, A.; Kessel, D.; Korbelik, M.; Moan, J.; Mroz, P.; Nowis, D.; Piette, J.; Wilson, B. C.; Golab, J. Photodynamic Therapy of Cancer: An Update. *CA Cancer J. Clin.* **2011,** *61*, 250-281.

(8) Celli, J. P.; Spring, B. Q.; Rizvi, I.; Evans, C. L.; Samkoe, K. S.; Verma, S.; Pogue, B. W.; Hasan, T. Imaging and Photodynamic Therapy: Mechanisms, Monitoring, and Optimization. *Chem. Rev.* **2010,** *110*, 2795-2838.

(9) Li, X.; Lee, S.; Yoon, J. Supramolecular Photosensitizers Rejuvenate Photodynamic Therapy. *Chem. Soc. Rev.* **2018,** *47*, 1174-1188.

(10) Castano, A. P.; Mroz, P.; Hamblin, M. R. Photodynamic Therapy and Anti-Tumour Immunity. *Nat. Rev. Cancer* **2006,** *6*, 535-545.

(11) Li, X.; Kwon, N.; Guo, T.; Liu, Z.; Yoon, J. Innovative Strategies for Hypoxic-Tumor Photodynamic Therapy. *Angew. Chem. Int. Ed.* **2018,** *57*, 11522-11531.

(12) Wilson, W. R.; Hay, M. P. Targeting Hypoxia in Cancer Therapy. *Nat. Rev. Cancer* **2011,** *11*, 393-410.

(13) Thomas, S.; Harding, M. A.; Smith, S. C.; Overdevest, J. B.; Nitz, M. D.; Frierson, H. F.; Tomlins, S. A.; Kristiansen, G.; Theodorescu, D. CD24 Is an Effector of HIF-1–Driven Primary Tumor Growth and Metastasis. *Cancer Res.* **2012,** *72*, 5600-5612.

(14) Wang, S.; Gu, K.; Guo, Z.; Yan, C.; Yang, T.; Chen, Z.; Tian, H.; Zhu, W.-H. Self-Assembly of a Monochromophore-Based Polymer Enables Unprecedented Ratiometric Tracing of Hypoxia. *Adv. Mater.* **2019,** *31*, 1805735.

(15) Teicher, B. A. Hypoxia and Drug Resistance. *Cancer Metastasis Rev.* **1994,** *13*, 139-168.

(16) Song, G.; Ji, C.; Liang, C.; Song, X.; Yi, X.; Dong, Z.; Yang, K.; Liu, Z. TaOx Decorated Perfluorocarbon Nanodroplets as Oxygen Reservoirs to Overcome Tumor Hypoxia and Enhance Cancer Radiotherapy. *Biomaterials* **2017,** *112*, 257-263.

(17) Zhou, J.; Xue, C.; Hou, Y.; Li, M.; Hu, Y.; Chen, Q.; Li, Y.; Li, K.; Song, G.; Cai, K.; Luo, Z. Oxygenated Theranostic Nanoplatforms with Intracellular Agglomeration Behavior for Improving the Treatment Efficacy of Hypoxic Tumors. *Biomaterials* **2019,** *197*, 129-145.

(18) Huang, C. C.; Chia, W. T.; Chung, M. F.; Lin, K. J.; Hsiao, C. W.; Jin, C.; Lim, W. H.; Chen, C. C.; Sung, H. W. An Implantable Depot That Can Generate Oxygen *in Situ* for Overcoming Hypoxia-Induced Resistance to Anticancer Drugs in Chemotherapy. *J. Am. Chem. Soc.* **2016,** *138*, 5222-5225.

(19) Zhang, R.; Song, X.; Liang, C.; Yi, X.; Song, G.; Chao, Y.; Yang, Y.; Yang, K.; Feng, L.; Liu, Z. Catalase-Loaded Cisplatin-Prodrug-Constructed Liposomes to Overcome Tumor Hypoxia for Enhanced Chemo-Radiotherapy of Cancer. *Biomaterials* **2017,** *138*, 13-21.

(20) Song, G.; Chen, Y.; Liang, C.; Yi, X.; Liu, J.; Sun, X.; Shen, S.; Yang, K.; Liu, Z. Catalase-Loaded TaOx Nanoshells as Bio-Nanoreactors Combining High-Z Element and Enzyme Delivery for Enhancing Radiotherapy. *Adv. Mater.* **2016,** *28*, 7143-7148.

(21) Liu, C. P.; Wu, T. H.; Liu, C. Y.; Chen, K. C.; Chen, Y. X.; Chen, G. S.; Lin, S. Y. Self-Supplying O_2 through the Catalase-Like Activity of Gold Nanoclusters for Photodynamic Therapy against Hypoxic Cancer Cells. *Small* **2017,** *13*, 1700278.

(22) Yang, G.; Zhang, R.; Liang, C.; Zhao, H.; Yi, X.; Shen, S.; Yang, K.; Cheng, L.; Liu, Z. Manganese Dioxide Coated WS_2@Fe_3O_4/sSiO_2 Nanocomposites for pH-Responsive MR Imaging and Oxygen-Elevated Synergetic Therapy. *Small* **2018,** *14*, 1702664.

(23) Gong, H.; Chao, Y.; Xiang, J.; Han, X.; Song, G.; Feng, L.; Liu, J.; Yang, G.; Chen, Q.; Liu, Z. Hyaluronidase to Enhance Nanoparticle-Based Photodynamic Tumor Therapy. *Nano Lett.* **2016,** *16*, 2512-2521.

(24) Chen, Q.; Chen, J.; Liang, C.; Feng, L.; Dong, Z.; Song, X.; Song, G.; Liu, Z. Drug-Induced Co-Assembly of Albumin/Catalase as Smart Nano-Theranostics for Deep Intra-Tumoral Penetration, Hypoxia Relieve, and Synergistic Combination Therapy. *J. Controlled Release* **2017,** *263*, 79-89.

(25) Szatrowski, T. P.; Nathan, C. F. Production of Large Amounts of Hydrogen Peroxide by Human Tumor Cells. *Cancer Res.* **1991,** *51*, 794-798.

(26) Muz, B.; de la Puente, P.; Azab, F.; Azab, A. K. The Role of Hypoxia in Cancer Progression, Angiogenesis, Metastasis, and Resistance to Therapy. *Hypoxia* **2015,** *3*, 83-92.

(27) Yu, M.; Wu, J.; Shi, J.; Farokhzad, O. C. Nanotechnology for Protein Delivery: Overview and Perspectives. *J. Controlled Release* **2016,** *240*, 24-37.

(28) Gu, Z.; Biswas, A.; Zhao, M.; Tang, Y. Tailoring Nanocarriers for Intracellular Protein Delivery. *Chem. Soc. Rev.* **2011,** *40*, 3638-3655.

(29) Scaletti, F.; Hardie, J.; Lee, Y.-W.; Luther, D. C.; Ray, M.; Rotello, V. M. Protein Delivery into Cells Using Inorganic Nanoparticle–Protein Supramolecular Assemblies. *Chem. Soc. Rev.* **2018,** *47*, 3421-3432.

(30) Tu, J.; Boyle, A. L.; Friedrich, H.; Bomans, P. H. H.; Bussmann, J.; Sommerdijk, N. A. J. M.; Jiskoot, W.; Kros, A. Mesoporous Silica Nanoparticles with Large Pores for the Encapsulation and Release of Proteins. *ACS Appl. Mater. Interfaces* **2016,** *8*, 32211-32219.

(31) Yang, J.-A.; Park, K.; Jung, H.; Kim, H.; Hong, S. W.; Yoon, S. K.; Hahn, S. K. Target Specific Hyaluronic Acid–Interferon Alpha Conjugate for the Treatment of Hepatitis C Virus Infection. *Biomaterials* **2011,** *32*, 8722-8729.

(32) Zhang, N.; Zhao, F.; Zou, Q.; Li, Y.; Ma, G.; Yan, X. Multitriggered Tumor-Responsive Drug Delivery Vehicles Based on Protein and Polypeptide Coassembly for Enhanced Photodynamic Tumor Ablation. *Small* **2016,** *12*, 5936-5943.

(33) Liu, K.; Xing, R.; Zou, Q.; Ma, G.; Möhwald, H.; Yan, X. Simple Peptide-Tuned Self-Assembly of Photosensitizers Towards Anticancer Photodynamic Therapy. *Angew. Chem. Int. Ed.* **2016,** *55*, 3036-3039.

(34) Li, S.; Zou, Q.; Li, Y.; Yuan, C.; Xing, R.; Yan, X. Smart Peptide-Based Supramolecular Photodynamic Metallo-Nanodrugs Designed by Multicomponent Coordination Self-Assembly. *J. Am. Chem. Soc.* **2018,** *140*, 10794-10802.

(35) Pisal, D. S.; Kosloski, M. P.; Balu-Iyer, S. V. Delivery of Therapeutic Proteins. *J. Pharm. Sci.* **2010,** *99*, 2557-2575.

(36) Qi, Y.; Chilkoti, A. Protein-Polymer Conjugation-Moving Beyond Pegylation. *Curr. Opin. Chem. Biol.* **2015,** *28*, 181-193.

(37) Mero, A.; Pasqualin, M.; Campisi, M.; Renier, D.; Pasut, G. Conjugation of Hyaluronan to Proteins. *Carbohydr. Polym.* **2013,** *92*, 2163-2170.

(38) Alconcel, S. N. S.; Baas, A. S.; Maynard, H. D. FDA-Approved Poly(Ethylene Glycol)–Protein Conjugate Drugs. *Polym. Chem.* **2011,** *2*, 1442-1448.

(39) Misra, S.; Heldin, P.; Hascall, V. C.; Karamanos, N. K.; Skandalis, S. S.; Markwald, R. R.; Ghatak, S. Hyaluronan–CD44 Interactions as Potential Targets for Cancer Therapy. *FEBS J.* **2011,** *278*, 1429-1443.

(40) Kim, H.; Jeong, H.; Han, S.; Beack, S.; Hwang, B. W.; Shin, M.; Oh, S. S.; Hahn, S. K. Hyaluronate and Its Derivatives for Customized Biomedical Applications. *Biomaterials* **2017,** *123*, 155-171.

(41) Götte, M.; Yip, G. W. Heparanase, Hyaluronan, and CD44 in Cancers: A Breast Carcinoma Perspective. *Cancer Res.* **2006,** *66*, 10233-10237.

(42) Mattheolabakis, G.; Milane, L.; Singh, A.; Amiji, M. M. Hyaluronic Acid Targeting of CD44 for Cancer Therapy: From Receptor Biology to Nanomedicine. *J. Drug Targeting* **2015,** *23*, 605-618.

(43) Zhu, Q.; Chen, X.; Xu, X.; Zhang, Y.; Zhang, C.; Mo, R. Tumor-Specific Self-Degradable Nanogels as Potential Carriers for Systemic Delivery of Anticancer Proteins. *Adv. Funct. Mater.* **2018,** *28*, 1707371.

(44) Wang, H.; Chao, Y.; Liu, J.; Zhu, W.; Wang, G.; Xu, L.; Liu, Z. Photosensitizer-Crosslinked *in-Situ* Polymerization on Catalase for Tumor Hypoxia Modulation & Enhanced Photodynamic Therapy. *Biomaterials* **2018,** *181*, 310-317.

(45) Bae, K. H.; Tan, S.; Yamashita, A.; Ang, W. X.; Gao, S. J.; Wang, S.; Chung, J. E.; Kurisawa, M. Hyaluronic Acid-Green Tea Catechin Micellar Nanocomplexes: Fail-Safe Cisplatin Nanomedicine for the Treatment of Ovarian Cancer without Off-Target Toxicity. *Biomaterials* **2017,** *148*, 41-53.

(46) Lin, W. J.; Lee, W. C.; Shieh, M. J. Hyaluronic Acid Conjugated Micelles Possessing CD44 Targeting Potential for Gene Delivery. *Carbohydr. Polym.* **2017,** *155*, 101-108.

(47) Webber, M. J.; Langer, R. Drug Delivery by Supramolecular Design. *Chem. Soc. Rev.* **2017,** *46*, 6600-6620.

(48) Maeda, H., The Enhanced Permeability and Retention (EPR) Effect in Tumor Vasculature: The Key Role of Tumor-Selective Macromolecular Drug Targeting. *Adv. Enzyme Regul.* **2001,** *41*, 189-207.

(49) Góth, L., A Simple Method for Determination of Serum Catalase Activity and Revision of Reference Range. *Clin. Chim. Acta* **1991,** *196*, 143-151.

(50) Allen, T. M.; Cullis, P. R. Drug Delivery Systems: Entering the Mainstream. *Science* **2004,** *303*, 1818-1822.

(51) Matsumura, Y.; Maeda, H. A New Concept for Macromolecular Therapeutics in Cancer Chemotherapy: Mechanism of Tumoritropic Accumulation of Proteins and the Antitumor Agent Smancs. *Cancer Res.* **1986,** *46*, 6387-6392.

(52) Xu, S.; Zhu, X.; Zhang, C.; Huang, W.; Zhou, Y.; Yan, D. Oxygen and Pt(II) Self-Generating Conjugate for Synergistic Photo-Chemo Therapy of Hypoxic Tumor. *Nat. Commun.* **2018,** *9*, 2053.

(53) Halliwell, B.; Clement, M. V.; Long, L. H. Hydrogen Peroxide in the Human Body. *FEBS Lett.* **2000,** *486*, 10-13.

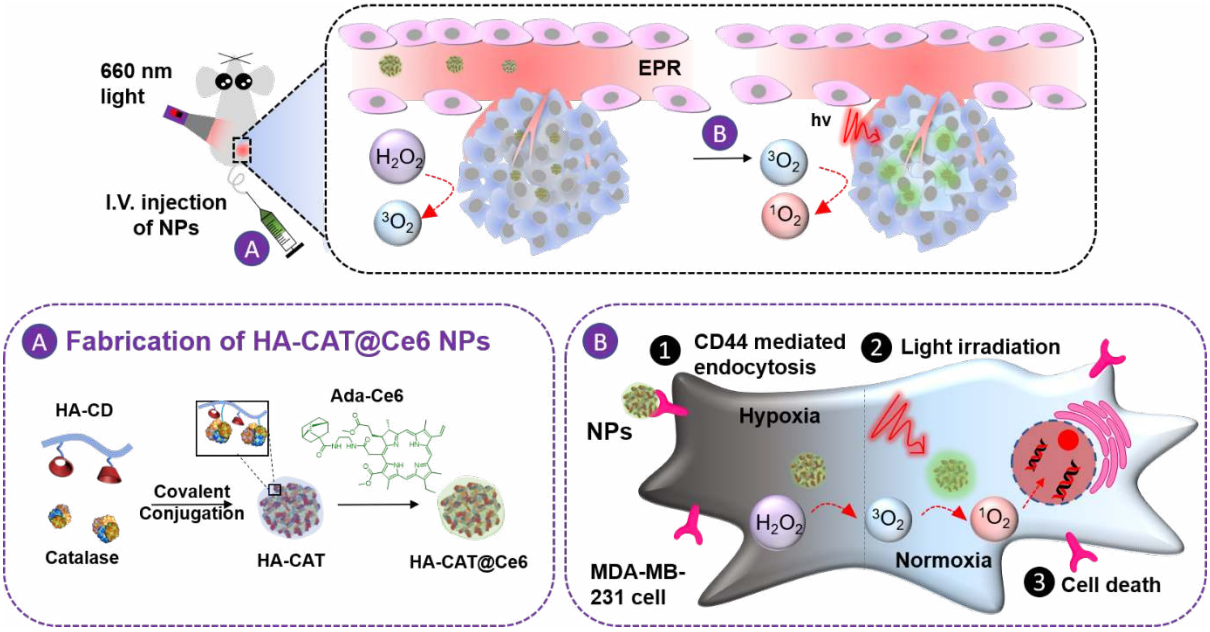

Scheme 1. Schematic illustration of the processes after intravenous injection of HA-CAT@aCe6 NPs into tumor-bearing mice. Process A: HA-CAT@aCe6 NPs were prepared by the conjugation of cyclodextrin modified HA with catalase, followed by supramolecular encapsulation of aCe6. Process B: HA-CAT@aCe6 NPs accumulate in hypoxic tumor and catalyze intracellular H_2O_2 to ground state oxygen $^3O_2$. $^3O_2$ is then converted to singlet oxygen $^1O_2$ upon 660 nm light irradiation for PDT of cancer.

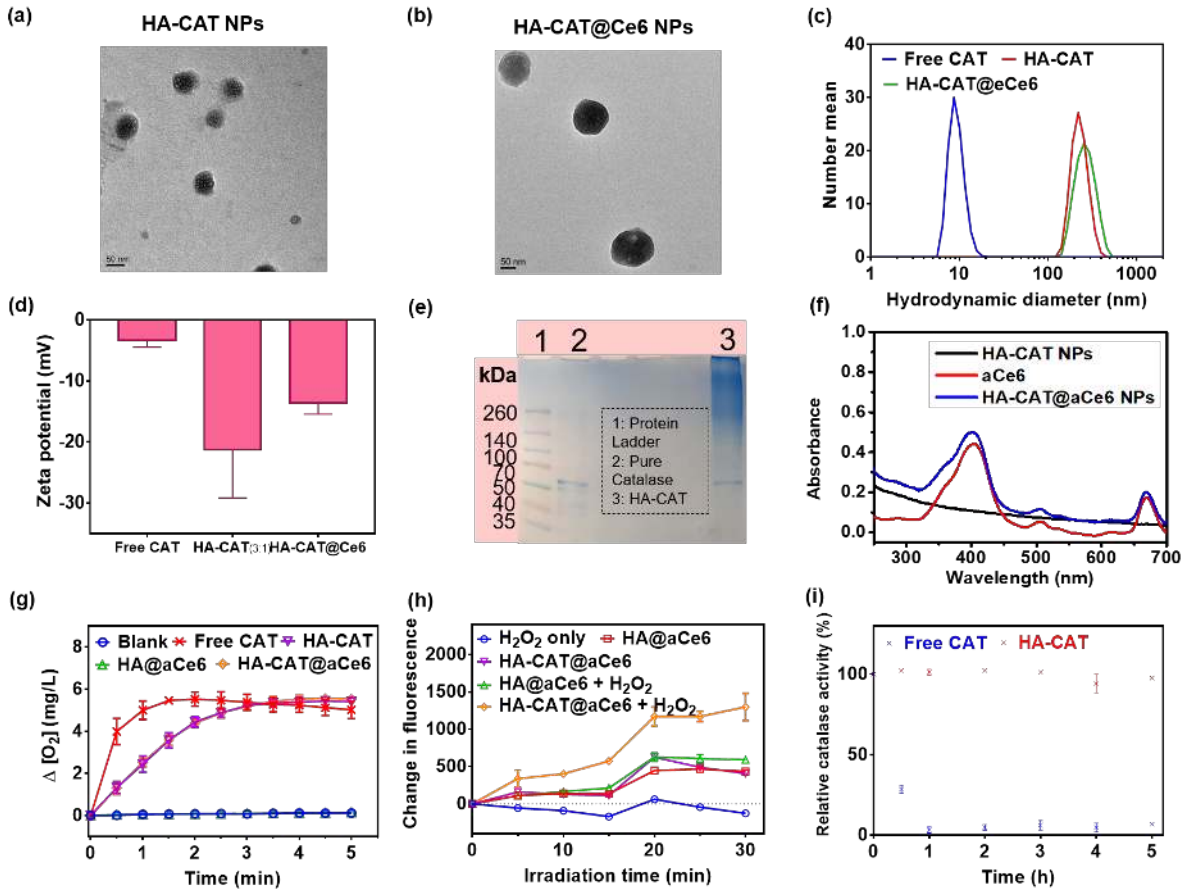

Figure 1. Characterizations of HA-CAT@aCe6 NPs. TEM images of (a) HA-CAT NPs and (b) HA-CAT@aCe6. (c) Hydrodynamic diameters measured from DLS of free catalase, HA-CAT NPs and HA-CAT@aCe6. (d) Zeta potential of free catalase, HA-CAT NPs and HA-CAT@aCe6. (e) SDS-PAGE of HA-CAT NPs. Lane 1 is the protein ladder corresponding to known mass protein. (f) Absorbance of aCe6, HA-CAT NPs, and HA-CAT@aCe6 NPs. (g) Change in oxygen concentration over time when different samples (H_2O_2 only, free catalase, HA-CAT, HA@aCe6, and HA-CAT@aCe6 NPs) were incubated with H_2O_2. (h) Change in fluorescence of SOSG upon irradiation time for H_2O_2 only, aCe6 with H_2O_2, HA-CAT@aCe6 only, and HA-CAT@aCe6 with H_2O_2. (i) Relative enzymatic activity of free catalase and HA-CAT@aCe6 incubated with proteinase K over 4 h. The data are reported in mean ± standard deviation in duplicates of three.

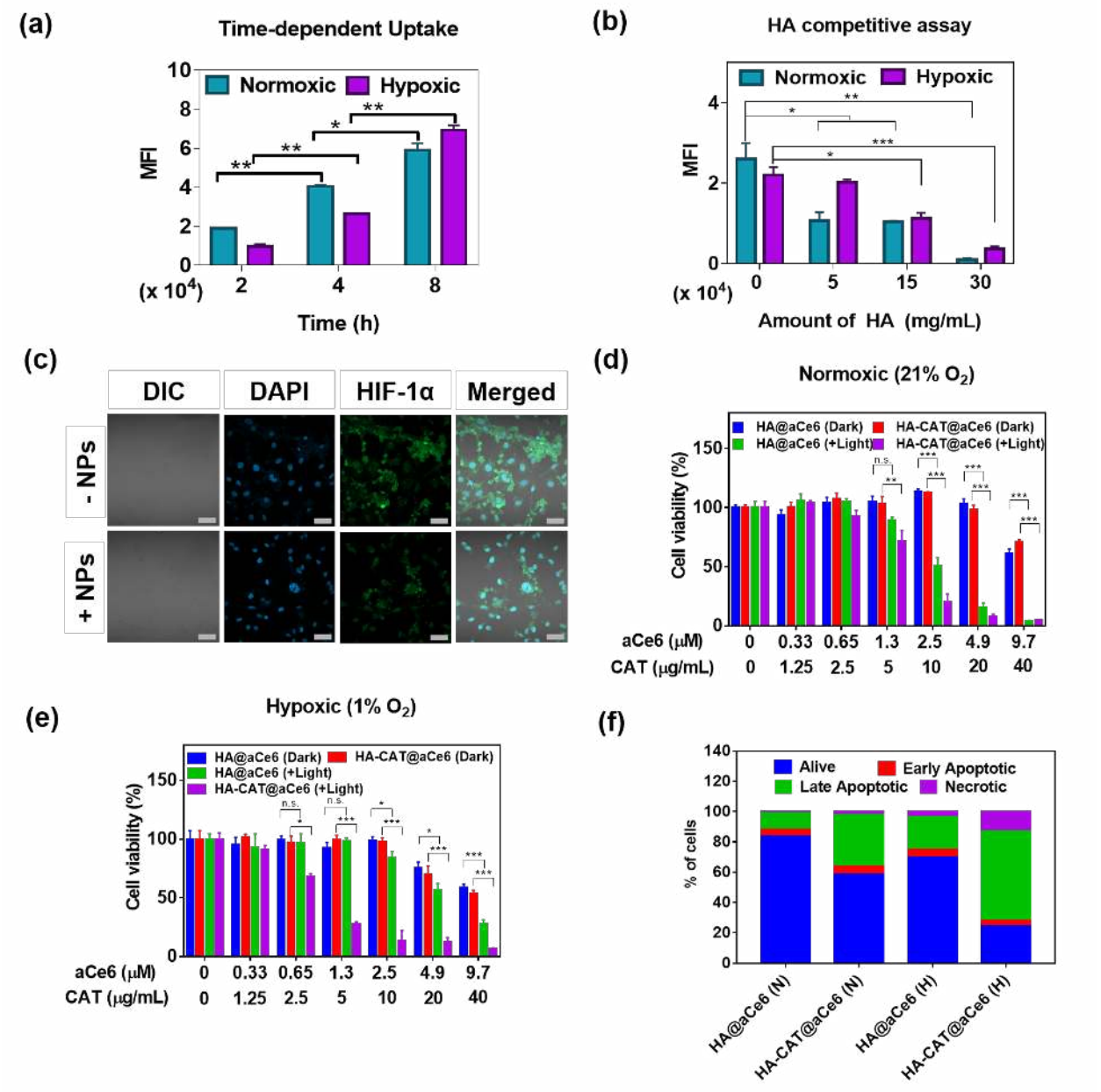

Figure 2. *In vitro* therapy on MDA-MB-231 cells. (a) MFI for time dependent uptake of HA-CAT@aCe6 NPs under normoxic and hypoxic conditions measured with flow cytometry. (b) MFI of HA-CAT@aCe6 NPs based on flow cytometric results under pretreatments with different amounts of free HA. (c) Fluorescence images of MDA-MB-231 cells immunostained for the detection of hypoxic marker HIF-1α after the incubation with and without HA-CAT@aCe6 NPs. Scale bar: 50 μm. DAPI: 4',6-diamidino-2-phenylindole. Cell viability of MDA-MB-231 cells

treated with HA-CAT@aCe6 NPs at different concentrations under (d) normoxic (21% O_2) and (e) hypoxic (1% O_2) conditions upon 660 nm light irradiation (5 mW cm^{-2}) for 5 min. (f) Different cell populations obtained from apoptotic study using Annexin V FITC and propidium iodide (PI) after the treatment with HA-CAT@aCe6 NPs, where [aCe6] = 0.65 μM and [catalase] = 2.5 μg/mL. The statistical analysis was carried out using Student's t test, * is when $p < 0.05$, ** is when $p < 0.01$ and *** is when $p < 0.005$.

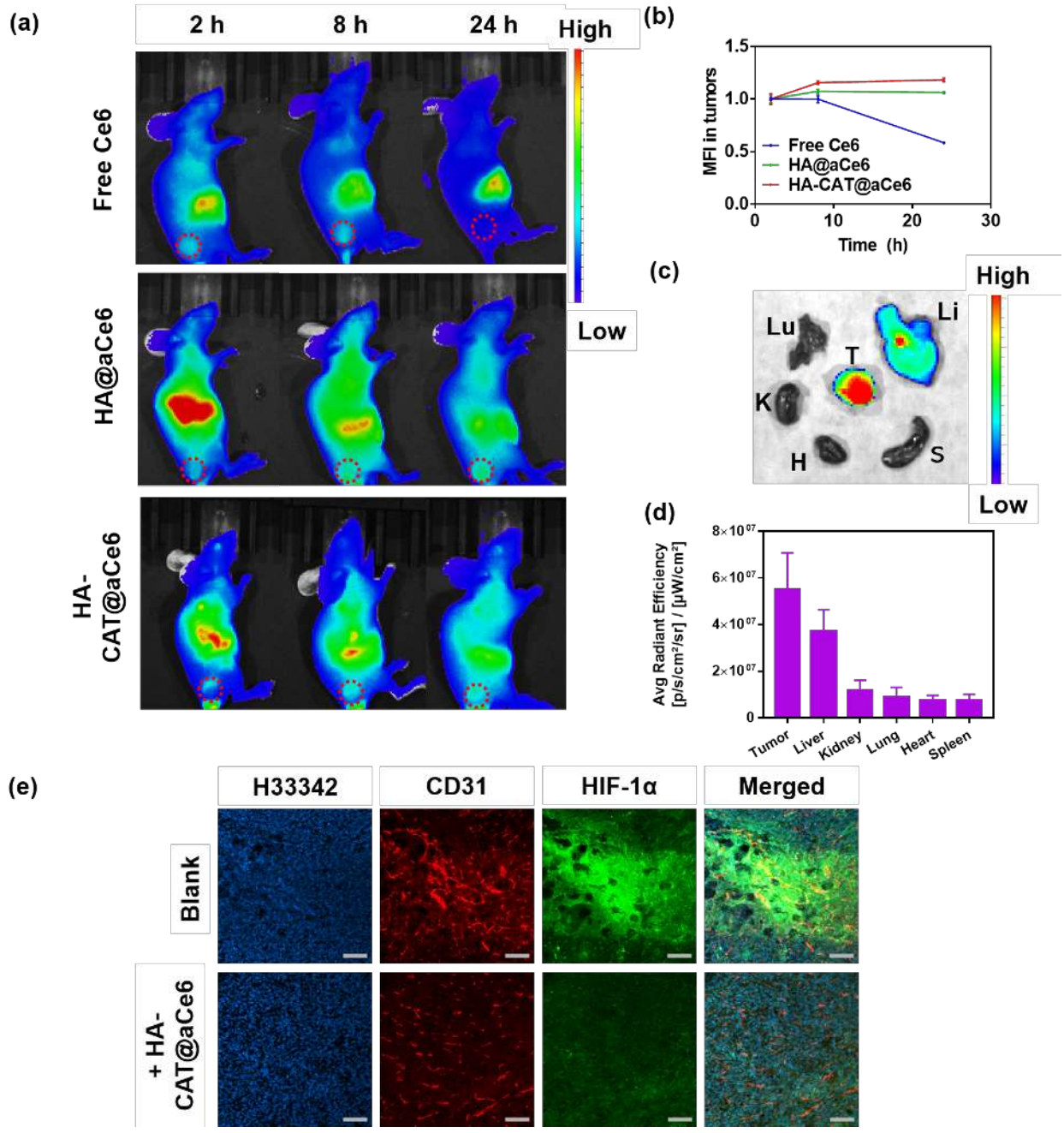

Figure 3. *In vivo* biodistribution of HA-CAT@aCe6 NPs. (a) Biodistribution of HA-CAT@aCe6 NPs in mice at time interval of 2 h, 8 h and 24 h after intravenous injection. Tumors are circled with red dashed lines. (b) Relative mean fluorescence intensity obtained from the images of tumors using ImageJ. (c) *Ex vivo* fluorescence image of various major organs and the tumor excised from mice at 24 h after intravenous injection of HA-CAT@aCe6 NPs. T, Li, S, H, K and Lu stand for

tumor, liver, spleen, heart, kidney and lung, respectively. (d) Average radiant efficiency of the organs and tumor from (c). (e) Immunofluorescence staining of tumor sections excised from mice after the treatment with PBS (control) and HA-CAT@aCe6 NPs. Nuclei of the cells were stained blue with Hoechst 33342, blood vessels were stained red with anti-CD31 antibody, and hypoxic tumor areas stained green with HIF-1α antibody. Scale bar: 100 μm.

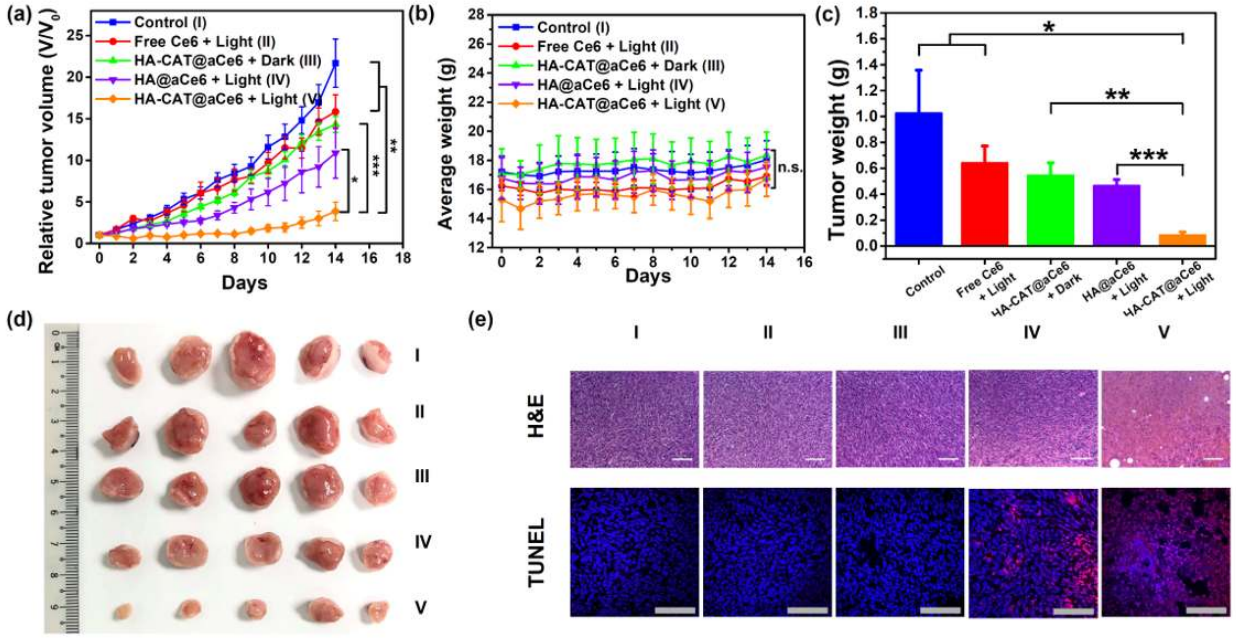

Figure 4. *In vivo* PDT. (a) Relative tumor volumes of MDA-MB-231 tumor-bearing mice with five treatment groups (I-V) over 14 days. (b) Average body weights of mice from these treatment groups. (c) Mean tumor weights of mice excised on the 14th day after these treatments. (d) Photos of excised tumors from mice on the 14th day after these treatments. (e) Histological analysis of tumor section stained with H&E and TUNEL from mice with different treatment groups. Nuclei were stained with DAPI (blue) and TUNEL (red). Scale bar: 100 μm. Light (660 nm, at 50 mW cm^{-2}) was irradiated for 20 min. Data were presented as mean ± standard error mean (SEM). *, $p \leq 0.05$; **, $p \leq 0.01$, ***, $p \leq 0.001$ as calculated by Student's t test.

TOC Graphic

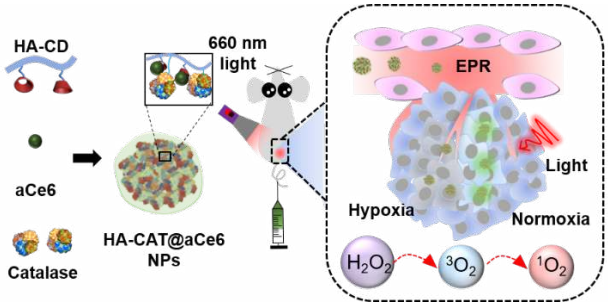
HA-CD
aCe6
Catalase
660 nm
light
HA-CAT@aCe6
NPs
EPR
Light
Hypoxia
Normoxia
H_2O_2
$^3O_2$
$^1O_2$